**Astronomy
&
Astrophysics**

Spectroscopic orbits and variations of RS Ophiuchi

E. Brandi[1,2,3], C. Quiroga[1,2], J. Mikołajewska[4], O. E. Ferrer[1,5], and L. G. García[1,2]

[1] Facultad de Ciencias Astronómicas y Geofísicas, Universidad Nacional de La Plata (UNLP), Argentina
   e-mail: ebrandi@fcaglp.unlp.edu.ar
[2] Instituto de Astrofísica de La Plata (CCT La Plata-CONICET-UNLP), Argentina
[3] Comisión de Investigaciones Científicas de la Provincia de Buenos Aires (CIC), Argentina
[4] Copernicus Astronomical Center, Warsaw, Poland
   e-mail: mikolaj@camk.edu.pl
[5] Consejo Nacional de Investigaciones Científicas y Técnicas (CONICET), Argentina

ABSTRACT

Aims. The aims of our study are to improve the orbital elements of the giant and to derive the spectroscopic orbit for the white dwarf companion of the symbiotic system RS Oph. Spectral variations related to the 2006 outburst are also studied.

Methods. We performed an analysis of about seventy optical and near infrared spectra of RS Oph that were acquired between 1998 and June 2008. The spectroscopic orbits were obtained by measuring the radial velocities of the cool component absorption lines and the broad Hα emission wings, which seem to be associated with the hot component. A set of cF-type absorption lines were also analyzed for a possible connection with the hot component motion.

Results. A new period of 453.6 days and a mass ratio, $q = M_g/M_h = 0.59 \pm 0.05$ were determined. Assuming a massive white dwarf as the hot component ($M_h = 1.2-1.4\ M_\odot$) the red giant mass is $M_g = 0.68-0.80\ M_\odot$ and the orbit inclination, $i = 49°-52°$. The cF-type lines are not associated with either binary component, and are most likely formed in the material streaming towards the hot component. We also confirm the presence of the Li I doublet in RS Oph and its radial velocities fit very well to the M-giant radial velocity curve. Regardless of the mechanism involved to produce lithium, its origin is most likely from within the cool giant rather than material captured by the giant at the time of the nova explosion.

The quiescent spectra reveal a correlation of the H I and He I emission line fluxes with the monochromatic magnitudes at 4800 Å, indicating that the hot component activity is responsible for those flux variations. We also discuss the spectral characteristics around 54–55 and 240 days after the 2006 outburst. In April 2006 most of the emission lines present a broad pedestal with a strong and narrow component at about -20 km s^{-1} and two other extended emission components at -200 and $+150$ km s^{-1}. These components could originate in a bipolar gas outflow supporting the model of a bipolar shock-heated shell expanding through the cool component wind perpendicularly to the binary orbital plane. Our observations also indicate that the cF absorption system was disrupted during the outburst, and restored about 240 days after the outburst, which is consistent with the resumption of accretion.

Key words. stars: binaries: symbiotic – stars: novae, cataclysmic variables – stars: individual: RS Oph – techniques: spectroscopic

1. Introduction

RS Oph is a recurrent symbiotic nova in which a white dwarf near the Chandrasekhar limit orbits inside the outer wind of a red giant. The system has had numerous recorded outbursts (1898, 1933, 1958, 1967, 1985). The most recent outburst began on 2006 February 12 and multifrequency observations confirmed the current model for the outburst in which the massive white dwarf accretes material from the red giant until a thermonuclear runaway ensues and high velocity gas is ejected from the white dwarf. Because the white dwarf is orbiting inside the outer layers/wind of the red giant, a strong shock structure is established around the system.

For RS Oph, Garcia (1986) made the first orbital period estimate of about 230 days, based on eight radial velocity measurements. Two sets of lines were considered: M star absorption features and absorption cores of Fe II emission lines due to a shell. He could not, however, derive the mass ratio. Oppenheimer & Mattei (1993) analysed intervals between outbursts in the AAVSO visual light curve and found the strongest periods ranged between 892 and 2283 days. Dobrzycka & Kenyon (1994, hereafter DK94) continued monitoring the radial velocities of RS Oph during quiescence. They also separated their echelle spectra into sets of M-type and A-type absorption lines, both of which resulted in a period of 460 days. The A-type radial velocity curve was shifted by 0.37 relative to the M giant solution and it was not associated with the hot component motion. They concluded that their results are more reasonable if they only considered the circular orbit of the cool giant. DK94 searched for periodic variations in photometric data of RS Oph collected during 1971–1983 and after the 1985 outburst. For both time intervals they found the light curve to be the superposition of a longer period variation ($P = 2178$ days) and a shorter variation ($P = 508$ days). The longer period was in agreement with $P = 2283$ days given by Oppenheimer & Mattei (1993) but it did not appear in their radial velocity analysis so it could not be associated with the orbital motion. Fifteen infrared radial velocities were used by Fekel et al. (2000, hereafter FJHS00) combined with the 47 optical velocities of DK94 in order to improve the orbital elements of the giant. FJHS00 fitted a new period of 455.72 days for a circular solution and eccentric orbits were rejected applying the test of Lucy & Sweeney (1971).

In this study, we have collected spectroscopic data of RS Oph from September 1998 until October 2006 and two Feros spectra

taken on May and June 2008 were also included in our analysis. Our observation closest to the eruption was obtained in April 2006.

We describe our observations in Sect. 2; in Sect. 3 we determine double-line spectroscopic orbits for RS Oph; in Sect. 4 spectral characteristics observed during quiescence are presented; in Sect. 5 we describe spectral changes during the active phase at 54–55 and 240 days after eruption and finally a brief discussion of our results and conclusions are given in Sect. 6.

2. Observations

2.1. Spectroscopy

Spectroscopic observations of RS Oph were performed with the 2.15 m "Jorge Sahade" telescope of CASLEO[1] (San Juan, Argentina), during 1998–2006. 65 spectra with resolution 12 000–15 000 were obtained with a REOSC echelle spectrograph using a Tek CCD 1024×1024 pixels. The CCD data were reduced with IRAF[2] packages CCDRED and ECHELLE and all the spectra were measured using the SPLOT task within IRAF.

To obtain the flux calibration, standard stars from Hamuy et al. (1992) and Hamuy et al. (1994) were observed each night. A comparison of the spectra of the standards suggests that the flux calibration errors are about 20% in the central part of each echelle order.

Two high resolution spectra were acquired in May and June 2008 with the Feros spectrograph mounted at the 2.2 m telescope at ESO, La Silla (Chile). An EEV CCD-44 with 2048×4096 pixels was used as the detector with a pixel size of $15 \times 15\ \mu$m and resolving power of $R = 60\,000$.

3. Spectroscopic orbits

Spectroscopic orbits of RS Oph were calculated using high resolution spectra collected at CASLEO during the period 1998–2006.

To obtain the radial velocities of the red giant we have measured M-type absorptions in the region $\lambda \sim 6000$–8000 Å, corresponding to Fe I, Ti I, Ni I, Si I, O I, Zr I, Co I, V I, Mg I and Gd II. We have also identified and measured absorption lines of singly ionized elements in the blue region of our spectra ($\lambda \sim 4000$–5800 Å), which resemble spectra of A–F supergiants. This set of absorption lines, called cF-absorptions, are believed to be linked to the hot companion (e.g. Mikołajewska & Kenyon 1992; Quiroga et al. 2002; Brandi et al. 2005). These are basically the same lines that are called A-type absorption lines by DK94. As the Fe II lines show very variable and complex profiles with emission components, only the stronger Ti II absorption lines were considered in our orbital solutions.

In both cases individual radial velocities were obtained by a Gaussian fit of the line profiles. A mean value was calculated for each spectrum and the resulting heliocentric velocities together with their standard errors and with the number of measured lines are given in Table 1. The published radial velocities of the M-giant were also included in the table.

Table 2 lists the resulting orbital solutions for the M-giant using only our radial velocities as well as our radial velocities combined with the DK94 and FJHS00 data and considering in this case weighted values of radial velocities. We have applied a weight of 1 to the FJHS00 data and weights 0.33, 0.67 and 1 when the errors are larger than 4, between 2 and 3 and less than 2, respectively, for both the DK94 and our data. But we noted that the weighted solutions show no important differences when a weight of 1 is applied to all the data.

A new orbital period of 453.6 ± 0.4 days was determined. An elliptical orbit ($e = 0.14 \pm 0.03$) fits the measured velocities slightly better than a circular one (see Fig. 1a).

We have also determined the radial velocities from the broad emission wings of Hα which should reflect the motion of the hot component if the wings were formed in the inner region of the accretion disk or in an extended envelope near the hot component. For this we have used the method outlined by Schneider & Young (1980, for more details see Quiroga et al. 2002). This method consists of convolving the data with two identical Gaussian bandpasses whose centers have a separation of $2b$ with standard deviation σ. We have experimented with a range of values for b and σ fixed at 3 Å, for which we have obtained the circular orbit solutions. Figure 2 shows the dependence of the standard error σ_K of the orbital semi-amplitude K, and the σ_K/K ratio, as a function of b. It is noticeable that σ_K and σ_K/K increases sharply for b larger than ~ 7 Å. We can attribute these large standard errors to the velocity measurements dominated by the noise in the continuum rather than by the extreme high velocity wings of the line profile. We have therefore adopted $b = 7$ Å as the best value. The heliocentric radial velocities of the broad emission wings of Hα are included in Table 1.

The broad emission line wings of Hα show a mean velocity similar to the red giant systemic velocity (see Fig. 1b). They are clearly in antiphase with the M-giant curve, which suggests that they are really formed in a region very near to the hot component.

Finally we have calculated the combined orbital solutions from the M-giant absorptions and from the Hα broad emission wings (see Table 2). From a comparison of the variances of the velocities of the two individual solutions, weights of 0.64 and 1 were given to the Hα wings and the M-giant velocities, respectively. Leaving the period as a free parameter and taking a circular orbit, the best solution corresponds to a similar period of 454.1 ± 0.41 days and adopting the period 453.6 days, the best combined solution leads to a lower eccentricity, $e = 0.04 \pm 0.03$. Moreover, we have considered binned data of radial velocities taking phase intervals of 0.05, and as it is shown in Table 2, very similar results were obtained. These solutions show clear antiphase variations of both sets of radial velocities and the systemic velocity agrees very well with that of the cool component orbital solutions. The combined unbinned and binned solutions are shown in Figs. 1c and d, respectively.

Using the combined circular solutions for unbinned data, we have estimated the mass ratio $q = M_g/M_h = 0.59 \pm 0.05$, the component masses $M_g \sin^3 i = 0.35\ M_\odot$ and $M_h \sin^3 i = 0.59\ M_\odot$, and the binary separation $a \sin i = 240\ R_\odot$. Assuming that the hot component is a massive white dwarf close to the Chandrasekhar limit ($M_h = 1.2$–$1.4\ M_\odot$), we estimate the red giant mass, $M_g = 0.68$–$0.80\ M_\odot$ and the orbit inclination, $i = 49°$–$52°$, which is consistent with the absence of eclipses in both, the optical light curve and the H I and He I emission line fluxes in our spectra.

A lower limit for the mass ratio can be also derived from the ratio of the rotational velocity to the orbital semiamplitude

Table 1. Radial velocities of the M-giant component, Hα-wings and cF-absorptions in RS Oph.

JD 2 400 000+	Phase (†)	M-giant RV (km s^{-1})	(O−C)	Hα-wings RV (km s^{-1})	(O−C)	cF-abs RV (km s^{-1})	Source
45 035.038	−0.019	−41.0	0.0				DK94
45 063.017	0.043	−32.0	2.5				DK94
45 063.963	0.045	−35.0	−0.7				DK94
45 097.923	0.120	−27.4	−0.1				DK94
45 426.977	0.845	−41.1	11.9				DK94
45 426.993	0.845	−41.6	11.4				DK94
45 513.743	0.037	−36.6	−1.5				DK94
46 538.993	0.297	−29.0	−6.8				DK94
46 540.952	0.301	−32.0	−9.6				DK94
46 602.834	0.438	−40.7	−8.9				DK94
46 605.743	0.444	−39.3	−6.8				DK94
46 608.764	0.451	−39.4	−6.3				DK94
46 635.720	0.510	−37.6	1.8				DK94
46 691.608	0.633	−54.1	−3.0				DK94
46 867.010	0.020	−38.0	−1.1				DK94
46 891.957	0.075	−34.9	−3.7				DK94
46 895.935	0.084	−33.9	−3.5				DK94
46 918.913	0.134	−32.2	−6.0				DK94
46 929.994	0.159	−27.7	−3.2				DK94
46 953.833	0.211	−23.5	−1.3				DK94
46 979.733	0.268	−25.8	−4.1				DK94
47 312.835	0.003	−39.3	−0.6				DK94
47 313.822	0.005	−38.6	−0.1				DK94
47 486.561	0.386	−38.2	−11.0				DK94
47 719.764	0.900	−59.2	−10.2				DK94
47 777.656	0.028	−36.0	0.1				DK94
47 787.683	0.050	−37.4	−3.6				DK94
47 811.576	0.102	−30.5	−1.8				DK94
47 967.019	0.445	−29.5	3.1				DK94
47 992.928	0.502	−43.9	−5.4				DK94
48 016.933	0.555	−44.5	−0.4				DK94
48 048.826	0.625	−54.3	−3.8				DK94
48 349.954	0.289	−22.8	−0.8				DK94
48 368.857	0.331	−21.2	2.4				DK94
48 400.832	0.401	−20.1	8.4				DK94
48 411.892	0.426	−30.3	0.4				DK94
48 429.805	0.465	−38.5	−3.9				DK94
48 695.025	0.050	−39.5	−5.8				DK94
48 723.000	0.112	−30.6	−2.7				DK94
48 754.922	0.182	−28.9	−5.6				DK94
48 782.831	0.244	−34.3	−12.7				DK94
48 816.771	0.318	−29.5	−6.5				DK94
48 872.718	0.442	−34.7	−2.5				DK94
48 909.584	0.523	−44.4	−3.6				DK94
49 106.948	0.958	−42.8	0.7				DK94
49 136.907	0.024	−36.6	−0.2				DK94
49 174.784	0.108	−30.4	−2.1				DK94
49 998.639	0.924	−49.1	−2.3				FJHS00
50 162.905	0.286	−18.0	4.0				FJHS00
50 254.723	0.488	−33.5	3.6				FJHS00
50 320.643	0.634	−48.5	2.6				FJHS00
50 387.593	0.781	−61.9	−6.4				FJHS00
50 568.854	0.181	−27.5	−4.2				FJHS00
50 627.799	0.311	−19.3	3.4				FJHS00
50 751.574	0.584	−49.6	−2.7				FJHS00
50 933.851	0.986	−42.1	−1.5				FJHS00
50 981.817	0.091	−27.5	2.2				FJHS00
50 983.747	0.096	−26.8	2.5				FJHS00
51 051.677	0.245	−19.7	1.9				FJHS00
51 064.570	0.274			−40.7	8.0		CASLEO
51 066.532	0.278	−18.4 ± 8.3 (4)	3.4			−23.3 ± 1.2 (3)	CASLEO
51 069.467	0.285	−15.3 ± 5.4 (4)	6.6			−28.7 ± 3.5 (6)	CASLEO
51 069.537	0.285	−13.9 ± 7.5 (4)	8.0			−24.4 ± 4.9 (5)	CASLEO
51 069.571	0.285	−18.6 ± 5.7 (5)	3.3			−26.7 ± 3.6 (5)	CASLEO
51 106.592	0.367	−27.4	−1.7				FJHS00

Table 1. continued.

JD 2 400 000+	Phase (†)	M-giant RV (km s^{-1})	(O−C)	Hα-wings RV (km s^{-1})	(O−C)	cF-abs RV (km s^{-1})	Source
51 294.889	0.782	−63.5	−8.0				FJHS00
51 324.666	0.847	−55.3 ± 5.7 (24)	−2.5	−32.8	−2.5	−30.2 ± 3.7 (4)	CASLEO
51 324.678	0.847	−53.1 ± 2.1 (21)	−0.3	−34.2	−3.9	−30.1 ± 2.5 (5)	CASLEO
51 324.690	0.847	−54.6 ± 2.0 (20)	−1.8	−32.1	1.8	−24.9 ± 3.3 (3)	CASLEO
51 363.664	0.933	−45.0	0.9				FJHS00
51 422.584	0.063	−33.6 ± 1.4 (9)	−1.2	−49.6	−7.2	−34.4 ± 1.2 (7)	CASLEO
51 422.599	0.063	−29.5 ± 2.1 (6)	2.9	−46.2	−3.8	−36.2 ± 2.5 (7)	CASLEO
51 628.861	0.518	−37.5 ± 1.7 (31)	2.7	−39.7	−2.0	−42.4 ± 1.8 (7)	CASLEO
51 628.870	0.518	−38.4 ± 1.7 (28)	1.8	−38.3	−0.6	−44.0 ± 2.0 (6)	CASLEO
51 629.850	0.520	−39.6 ± 2.2 (22)	0.9	−38.9	−1.3	−40.6 ± 3.1 (7)	CASLEO
51 629.859	0.520	−39.8 ± 1.5 (28)	0.7	−38.9	−1.3	−43.6 ± 2.4 (7)	CASLEO
51 629.868	0.520	−39.6 ± 1.9 (26)	0.9	−38.9	−1.3	−43.9 ± 2.7 (6)	CASLEO
51 629.876	0.520	−40.7 ± 2.0 (26)	−0.2	−36.0	1.6	−43.5 ± 3.3 (6)	CASLEO
51 630.809	0.522	−37.6 ± 1.8 (27)	3.1	−33.1	4.4	−47.2 ± 0.5 (4)	CASLEO
51 630.832	0.522	−39.0 ± 2.2 (22)	1.7	−31.5	6.0	−46.7 ± 3.4 (5)	CASLEO
51 754.660	0.795	−59.4 ± 3.8 (6)	−4.3	−27.4	1.5	−29.4 ± 1.6 (7)	CASLEO
51 754.669	0.795	−58.7 ± 3.8 (6)	−3.6	−29.1	−0.2	−30.1 ± 2. (6)	CASLEO
51 754.680	0.795	−57.7 ± 4.1 (6)	−2.6	−27.8	1.1	−26.5 ± 2.5 (7)	CASLEO
51 790.615	0.874	−52.4 ± 2.9 (10)	−1.4	−34.2	−2.9	−18.6 ± 0.7 (7)	CASLEO
51 790.623	0.874	−53.1 ± 2.7 (9)	−2.1	−34.0	−2.7	−19.1 ± 1.1 (6)	CASLEO
51 790.630	0.874	−50.2 ± 3.8 (9)	0.8	−33.9	−2.6	−20.2 ± 1.7 (7)	CASLEO
51 791.616	0.877	−48.4 ± 1.1 (42)	2.4	−23.2	8.2		CASLEO
51 791.623	0.877	−46.7 ± 1.3 (39)	4.2	−23.7	7.7		CASLEO
51 791.630	0.877	−47.4 ± 1.3 (39)	3.5	−23.5	7.9		CASLEO
51 798.524	0.892	−54.8 ± 2.1 (7)	−5.1	−29.0	3.2	−18.6 ± 4.0 (7)	CASLEO
51 798.533	0.892	−54.8 ± 2.5 (6)	−5.1	−26.9	5.3	−22.1 ± 1.4 (6)	CASLEO
51 824.502	0.949	−40.8 ± 1.3 (10)	3.6	−29.1	6.2	−32.7 ± 1.1 (7)	CASLEO
51 824.511	0.949	−38.5 ± 1.9 (9)	5.9	−28.9	6.4	−32.7 ± 1.6 (7)	CASLEO
51 824.520	0.949	−41.4 ± 1.9 (10)	3.0	−28.5	6.8	−33.7 ± 1.3 (6)	CASLEO
51 827.511	0.956	−40.4 ± 1.2 (39)	3.3	−30.0	5.7		CASLEO
51 827.518	0.956	−39.0 ± 1.1 (38)	4.7	−30.2	5.5		CASLEO
51 827.526	0.956	−41.2 ± 1.3 (38)	2.5	−30.2	5.5		CASLEO
52 016.843	0.373	−19.8 ± 2.4 (11)	6.4	−51.5	−5.4	−32.4 ± 1.5 (7)	CASLEO
52 016.853	0.373	−24.8 ± 1.8 (6)	1.4	−52.2	−6.1	−32.3 ± 2.6 (7)	CASLEO
52 016.861	0.373	−24.3 ± 4.6 (5)	1.9	−49.4	−3.3	−35.6 ± 1.6 (6)	CASLEO
52 058.859	0.466	−36.6 ± 4.3 (9)	−1.9	−34.8	6.2		CASLEO
52 058.867	0.466	−37.9 ± 9.7 (6)	−3.2	−34.3	6.7		CASLEO
52 058.875	0.466	−34.0 ± 2.1 (2)	0.7	−38.3	2.7		CASLEO
52 059.853	0.468	−33.5 ± 1.2 (36)	1.4				CASLEO
52 059.861	0.468	−34.0 ± 1.1 (33)	0.9	−39.0	1.9		CASLEO
52 059.869	0.468	−34.3 ± 1.1 (32)	0.6	−40.1	0.8		CASLEO
52 132.575	0.628	−60.7 ± 1.2 (7)	−10.0	−34.1	−2.6	−41.8 ± 5.1 (6)	CASLEO
52 132.584	0.628	−61.0 ± 2.0 (7)	−10.3	−35.0	−3.5	−42.1 ± 5.1 (6)	CASLEO
52 388.895	0.193	−26.8 ± 1.0 (89)	−4.0	−50.5	−2.4	−33.5 ± 0.2 (2)	CASLEO
52 388.914	0.193	−24.4 ± 0.95 (93)	−1.6	−50.2	−2.1	−26.7 ± 1.2 (2)	CASLEO
52 529.553	0.504			−28.7	10.0		CASLEO
52 531.543	0.508	−38.7 ± 1.3 (122)	0.5	−32.7	5.7		CASLEO
52 531.556	0.508	−37.7 ± 1.3 (123)	1.5	−33.7	4.7		CASLEO
52 770.858	0.036	−34.5 ± 1.6 (70)	0.7	−28.7	12.0	−26.9 ± 2.2 (3)	CASLEO
52 770.873	0.036	−37.2 ± 1.8 (68)	−2.0	−29.2	11.5	−26.1 ± 0.4 (3)	CASLEO
52 771.837	0.038	−36.6 ± 3.2 (29)	−1.6	−35.5	5.3	−26.9 ± 1.8 (6)	CASLEO
52 771.846	0.038	−37.2 ± 3.3 (24)	−2.2	−36.6	4.2	−25.3 ± 1.8 (6)	CASLEO
52 772.848	0.040			−31.4	9.6		CASLEO
52 772.860	0.040			−30.7	10.3		CASLEO
52 887.575	0.292			−38.7	9.8		CASLEO
52 890.529	0.299	−21.6 ± 0.9 (110)	0.7	−34.4	14.0		CASLEO
52 890.542	0.299	−23.5 ± 0.9 (121)	−1.2	−34.9	13.5		CASLEO
53 126.836	0.820	−54.6 ± 1.4 (65)	−0.4			−26.5 ± 3.4 (5)	CASLEO
53 126.848	0.820	−54.5 ± 1.9 (55)	−0.3			−24.5 ± 1.6 (6)	CASLEO
53 127.850	0.822	−56.1 ± 1.1 (121)	−2.0	−30.9	−1.4		CASLEO
53 127.864	0.822	−54.2 ± 1.4 (119)	−0.1	−32.0	−2.5		CASLEO
53 476.884	0.592	−51.6 ± 1.7 (69)	−3.9	−28.0	5.3	−43.5 ± 2.7 (3)	CASLEO
53 476.897	0.592	−50.4 ± 1.5 (74)	−2.7	−25.4	7.9	−42.4 ± 2.4 (3)	CASLEO
53 479.879	0.599	−55.4 ± 1.3 (91)	−7.1	−36.4	−3.4		CASLEO
53 628.562	0.926	−51.1 ± 1.8 (32)	−4.5			−38.7 ± 2.7 (4)	CASLEO

Table 1. continued.

JD 2 400 000+	Phase (†)	M-giant RV (km s^{-1})	(O−C)	Hα-wings RV (km s^{-1})	(O−C)	cF-abs RV (km s^{-1})	Source
54 021.484	0.793	−57.2 ± 2.4 (58)	−2.0	−18.7	10.2	−25.3 ± 0.4 (3)	CASLEO
54 021.496	0.793	−57.1 ± 2.5 (66)	−1.9	−20.0	8.9	−24.2 ± 2.2 (4)	CASLEO

(†) We adopt the spectroscopic ephemeris: $T_{\mathrm{conj}} = 2\,445\,043.54 + 453.6\,E$.

Table 2. Orbital solutions of RS Oph.

Component	P [days]	K [km s^{-1}]	γ_0 [km s^{-1}]	e	ω [deg]	$T_0^{(1)}$ [JD 24...]	$\Delta\phi^{(2)}$	$a \sin i$ [AU]	$f(M)$ [$M_\odot$]
M-giant									
Our data	452.8 ± 1.5	19.5 ± 0.7	−38.0 ± 0.4	0$^{(3)}$		51 055.50		0.81	0.35
Our data	453.2 ± 1.2	20.0 ± 0.7	−38.7 ± 0.4	0.10 ± 0.03	120 ± 16	51 205.95		0.83	0.37
DK+F+ours	453.6 ± 0.4	17.5 ± 0.6	−39.5 ± 0.4	0$^{(3)}$		45 156.94	0.00	0.73	0.25
DK+F+ours	453.6$^{(3)}$	18.6 ± 0.6	−40.2 ± 0.4	0.14 ± 0.03	135 ± 11	44 873.23		0.77	0.29
cF-abs									
Our data$^{(5)}$	453.6$^{(3)}$	8.0 ± 1.2	−32.5 ± 0.9	0$^{(3)}$		50 493.51	−0.24	0.33	0.024
	453.6$^{(3)}$	10.2 ± 1.8	−31.8 ± 0.8	0.52 ± 0.14	200 ± 13	50 750.54		0.36	0.031
DK+ours	453.6$^{(3)}$	3.2 ± 0.9	−34.7 ± 0.7	0$^{(3)}$		45 041.11	−0.26	0.13	0.001
	453.6$^{(3)}$	8.3 ± 2.8	−34.6 ± 0.7	0.82 ± 0.07	344 ± 16	46 799.95		0.20	0.005
Emission wings									
Hα wings	456.0 ± 6.1	8.6 ± 1.2	−35.4 ± 0.70	0$^{(3)}$		50 376.11			
Hα wings	453.6$^{(3)}$	8.5 ± 1.2	−35.4 ± 0.70	0$^{(3)}$		50 385.80	0.53	0.42	0.029
Hα wings$^{(4)}$	453.6$^{(3)}$	10.0 ± 2.3	−36.6 ± 1.5	0$^{(3)}$				0.35	0.047

Combined orbital solutions ($P = 453.6 \pm 0.4$ days).

Component	K [km s^{-1}]	γ_0 [km s^{-1}]	e	ω [deg]	$T_0^{(1)}$ [JD24...]	$a \sin i$ [AU]	$M \sin^3 i$ [$M_\odot$]
DK+F+ours	17.1 ± 0.6	−38.7 ± 0.4	0$^{(3)}$		45 612.05	0.71	0.35
Hα wings	10.1 ± 1.2					0.42	0.59
DK+F+ours	17.2 ± 0.7	−38.7 ± 0.4	0.04 ± 0.03	87 ± 44	45 722.37	0.72	0.35
Hα wings	10.2 ± 1.2					0.42	0.59
DK+F+ours$^{(4)}$	16.4 ± 1.5	−38.4 ± 0.8	0$^{(3)}$		0.00	0.68	0.35
Hα wings$^{(4)}$	10.4 ± 1.8					0.43	0.55

Notes: $^{(1)}$ T_0 is the time of maximum velocity (circular orbits) or the time of periastron passage (elliptical orbits); $^{(2)}$ $\Delta\phi = (T_0 - T_{0,\mathrm{giant}})/P$; $^{(3)}$ assumed; $^{(4)}$ binned data; $^{(5)}$ solutions using only the measurements of the Ti II absorption lines.

of the red giant and assuming that the giant is synchronized. Adopting $v \sin i = 11.7 \pm 1.5$ km s^{-1} (Zamanov et al. 2007) and $K_g = 17.1 \pm 0.6$ km s^{-1} (Table 2) results in $q_{\min} = 0.68 \pm 0.1$. This lower limit is surprisingly close to the mass ratio derived from the radial velocity curves, and indicates that either the giant is filling its Roche lobe (RL) – the actual q should then be equal to $q_{\min}$ – or that its measured rotational velocity is faster than the synchronized value. The first possibility is favored by theoretically predicted synchronization and circularization time-scales for convective stars (Zahn 1977). It is also easier to ensure the high mass tranfer and accretion rate required by the activity and short nova outburst recurrence time of RS Oph. On the other hand, the presence of an RL-filling giant implies that the distance to RS Oph is a factor of 2 larger than generally accepted based on observational evidence (Barry et al. 2008).

The cF absorption lines do not trace clearly the orbit of the hot component. Any orbital solution leads to a significant eccentricity (see Table 2) and the radial velocity curve is shifted by ∼−0.26 P (0.74 P) relative to the M giant solution instead of 0.5 P (see Fig. 3). We think, in agreement with DK94, that in RS Oph the cF absorption lines are not associated with either binary component, and are most likely formed in the material streaming

towards the hot component. We note here that similar complications with the blue absorption system occurred for a few other active symbiotic systems. Mikołajewska & Kenyon (1996) failed to derive any radial velocity curve and orbital solution for the blue absorption system in Z And. In CI Cyg the radial velocities of the F-type absorption system suggest that their formation region is the material streaming from the giant near the hot component (Mikołajewska & Mikołajewski 1988), whereas a possible correlation between AR Pav's activity and the departures of the cF absorption velocities from the circular orbit suggests that this absorption system also may be affected by material streaming towards the hot component, presumably in a region where the stream encounters an accretion disk or an extended envelope around the hot component (Quiroga et al. 2002). We can see in Fig. 3 the departures of the cF-abs radial velocities from the circular orbit of the hot component due to a significant contribution from the stream.

In Figs. 1 and 3 and hereafter we adopt the period of 453.6 days and the origin of the phases corresponds to the inferior conjunction of the M-giant:

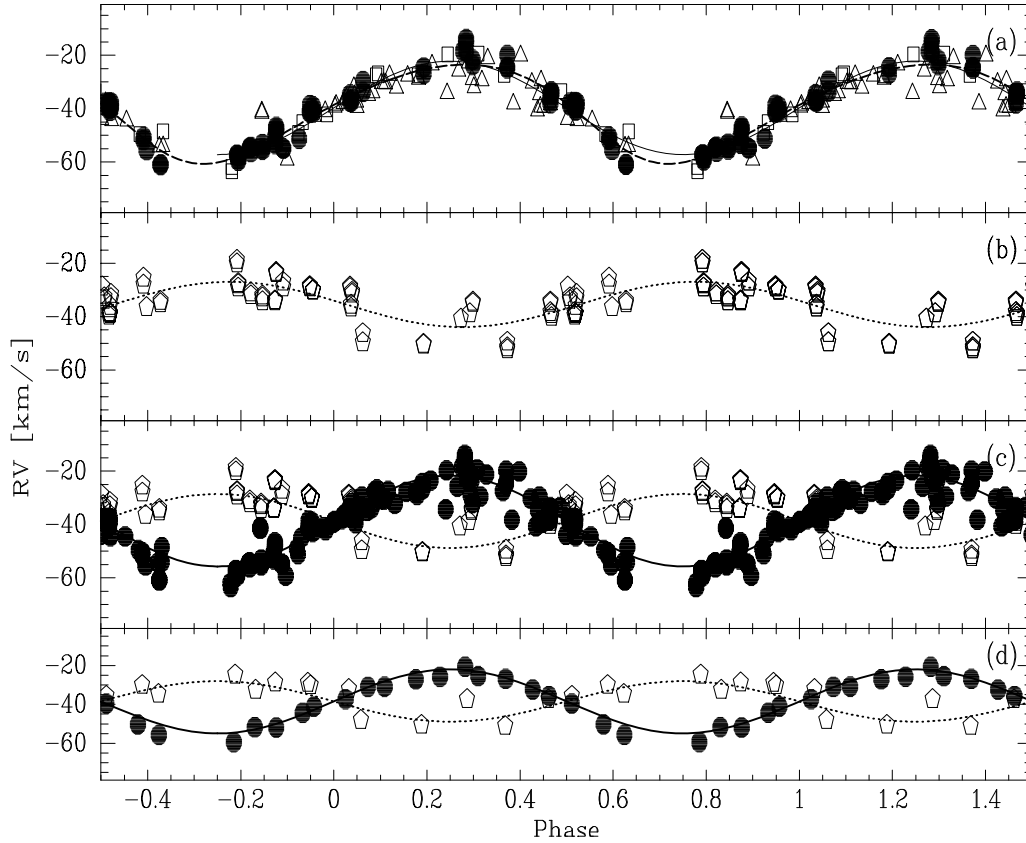$$T_{\mathrm{conj}} = \mathrm{JD}\ 2\,445\,043.54 \pm 5 + 453.6 \pm 0.4\,E.$$

Fig. 1. Radial velocity curves and orbital solutions for RS Oph. The data are phased with a period of 453.6 days and $T_{conj} = 2\,445\,043.54 \pm 5$ (the time of the inferior conjunction of the M giant). **a)** M-giant. Filled circles represent our data and open triangles and squares, the DK94 and FJHS00 data, respectively. The solid line gives the best circular fit and the dashed line gives the eccentric orbit ($e = 0.14$). **b)** The Hα wings (hereafter open symbols) and the best circular solution (dotted line). **c)** Combined circular solution for the M-giant (filled circles) and the Hα wings. **d)** The same with binned data.
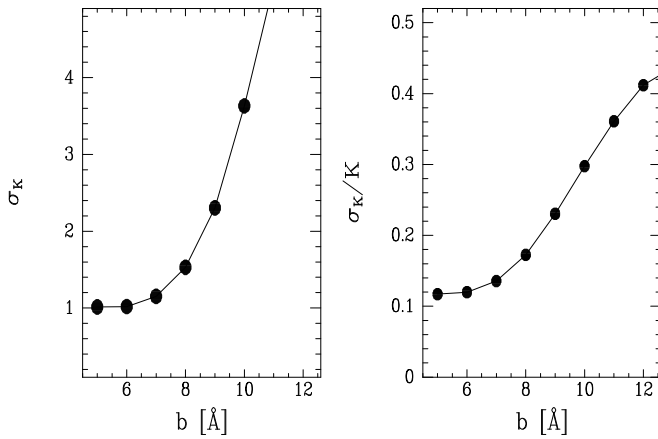
Fig. 2. The standard error of the orbital semi-amplitude σ_K and the σ_K/K ratio as a function of the parameter b. The best estimation of K is determined by the value of b where σ_K begins to sharply increase.

Fig. 3. Phased radial velocities of the cF-absorption lines (dots) and the best circular solution (solid line) for the hot component based on the Hα wings (*bottom*). The departures of the cF-abs radial velocities from the circular orbit of the hot component are due to a significant contribution from the gaseous stream between both stars. The residuals (O−C) are represented by empty circles whereas the solid and dashed lines mark the best circular solution for the hot and cool component, respectively (*top*).
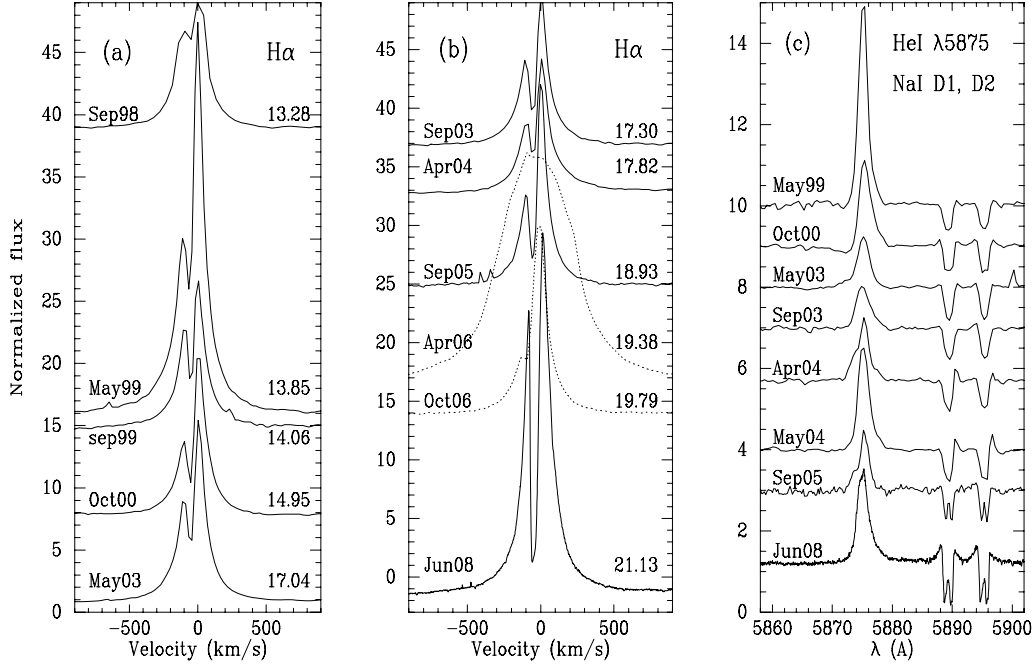
4. RS Oph at quiescence

Fluctuations in the fluxes of the emission lines and the continuum are observed during the period of quiescence covered by our observations. Several authors have previously reported such behaviour of RS Oph, outside the eruptive episodes (see Anupama & Mikołajewska 1999, and refences therein).

Fig. 4. Panels **a)** and **b)**: profiles of Hα. At quiescence the broad emission is cut by a central absorption which disappears during the outburst (dotted profile). Panel **c)**: profile variations of He I λ5875 and Na I doublet during the quiescent period. Blueshifted broad components in He I are present on April 2004 and September 2005. The Na I doublet shows weak emission components and double structure in absorption.

Table 3. Mean values of radial velocities and equivalent widths of the central absorptions in Hα and Hβ.

JD 2 450 000+	Phases (days)	Hα RV(km s^{-1})	eqw	Hβ RV(km s^{-1})	eqw
1069.6	13.285	−57.7	0.46	−25.6	0.43
1324.7	13.847	−56.6	0.59	−47.9	0.57
1422.6	14.063	−50.2	0.53	−43.0	0.72
1629.9	14.518	−48.8	0.71	−45.0	0.60
1754.7	14.795	−52.3	0.70	−46.9	0.58
1790.6	14.874	−52.4	0.73	−45.1	0.61
1791.6	14.877	−50.0	0.67		
1824.5	14.949	−50.7	0.74	−47.1	0.66
1827.5	14.956	−52.7	0.72		
2016.9	15.373	−48.4	0.75	−45.2	0.65
2059.9	15.468	−43.8	0.59	−47.8	0.60
2132.6	15.628	−48.1	0.62	−54.7	0.64
2388.9	16.193	−42.9	0.86	−43.4	
2531.6	16.508	−38.8	0.77		
2770.9	17.036	−48.4	0.63	−48.5	0.76
2771.8	17.038	−44.4	0.76	−41.1	0.86
2890.5	17.299	−50.1	0.86		
3126.8	17.820	−48.4	0.68	−40.8	0.56
3127.8	17.822	−47.3	0.83		
3476.9	18.592	−43.8	0.93	−42.9	0.75
3628.6	18.926	−51.1	0.92	−48.2	0.79
4600.8	21.070	−60.0	0.94	−54.5	0.88
4627.8	21.129	−43.6	1.07	−35.2	0.95

The spectra present essentially emission lines of H I, He I and [O I] at 6300 Å. In the observed members of the Balmer series, the broad emission is cut by a central absorption with a red peak always stronger than the blue one. Figure 4, left and central panels, show Hα profiles for several epochs. At quiescence the central absorption remains present although with variable intensity over the whole orbital cycle, whereas it disappears during the eruption, and it is weakly visible again in October 2006. The

radial velocity of the central absorption of Hα varies between −60 and −40 km s^{-1}. As it is shown in Fig. 5a this variation does not follow the motion of any stellar component of the system but Figs. 5b and c show changes of both the radial velocities and the equivalent widths with the different cycles of the binary, in the sense that the mean velocity was increasing until cycle 16 (May 2003) and then decreasing, whereas the equivalent widths were monotonically increasing.

The profile of Hβ also presents a double peak structure but the radial velocity of the central absorption is rather constant, without a clear variation with orbital phase or orbital cycle (see Figs. 5d–f).

Significant changes in the radial velocity of the central absorption in both Hα and Hβ were observed in the higher resolution Feros spectra between May and June 2008 (asterisks in Fig. 5). An explanation of this behaviour correlating the radial velocities with the flickering activity and the accretion processes in RS Oph is in progress.

Broad emission components were detected in the emission line He I λ5875 during April 2004 and September 2005 (see Fig. 4, right panel) at velocities of the order of ~100 km s^{-1}. The intensity of the He I emission lines and the presence of these broad components change quickly with a time scale of one or two days.

Figure 6 presents the Hα fluxes against the m_{4800} magnitudes calculated from our spectra. The figure shows that a clear correlation between both data exists, confirming that the emission line variability is correlated with the hot component activity (Anupama & Mikołajewska 1999).

4.1. Presence of the Li I λ6707 absorption line

One unsolved problem in astrophysics is the origin of lithium and other light elements in the universe. How and when lithium is depleted and an understanding of the processes controlling
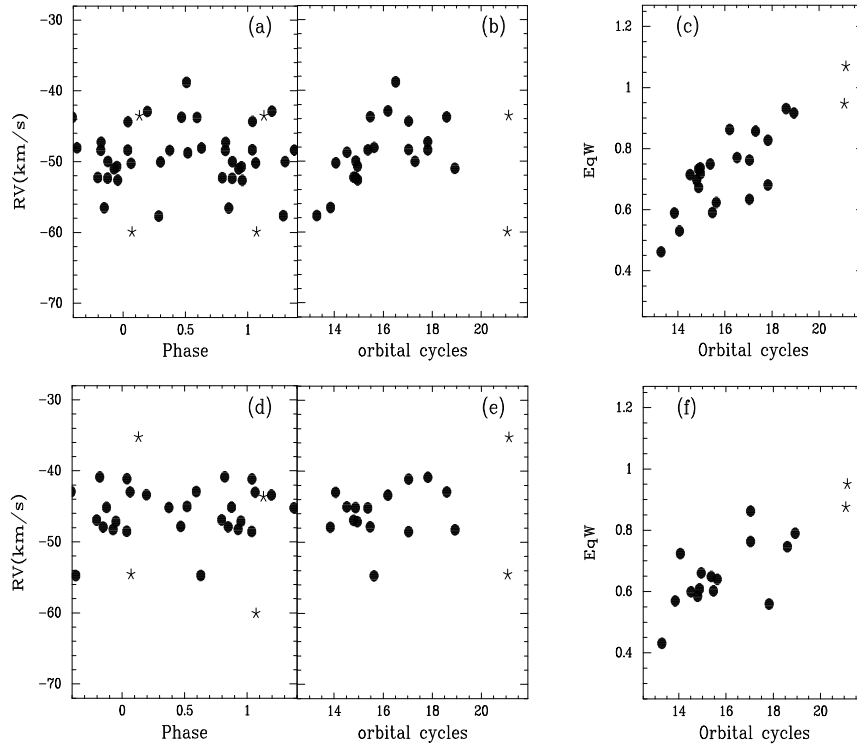
Fig. 5. Radial velocities and equivalent widths of the central absorptions of Hα (panels **a)–c)**) and Hβ (panels **d)–f)**) as a function of the orbital phases and the orbital cycles, respectively. Asterisks correspond to the Feros spectra.
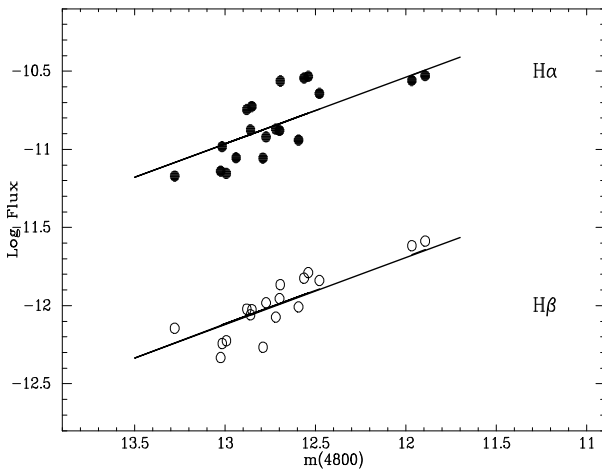

Fig. 6. Correlation of the Hα and Hβ emission line fluxes with the magnitudes at 4800 Å measured from our spectra.

lithium production are still not completely resolved. The synthesis of ^{7}Li in explosive hydrogen burning, in particular in accreting (CO or ONe) white dwarfs exploding as classical novae has been studied by several authors (see Jordi 2005, and references therein) and novae are predicted to be important sources of Galactic lithium.

However the observation of ^{7}Li in the ejecta of a nova outburst has been rather elusive. The Li I λ6708 line has been detected in the recurrent symbiotic novae T CrB (Shabhaz et al. 1999) and RS Oph (Wallerstein et al. 2006). Wallerstein et al.(2008) have recently derived Li abundances in these stars, $\log N(\text{Li}) = 1.2$ for RS Oph and 0.8 for T CrB, which are close to being solar. These Li abundances are however significantly

higher than those determined for most single K and M giants. Such high Li abundances are common in late-type secondaries in neutron and black hole binaries (e.g. Martin et al. 1994) but extremely rare in the symbiotic giants. In fact, the Li enhancement is thus far detected only in the symbiotic Mira V407 Cyg, where it can probably be explained as a consequence of hot bottom burning, which occurs in stars with initial masses in the range 4–6 $M_\odot$ (Tatarnikova et al. 2003). Such an explanation is, however, unlikely in the case of low mass, $\lesssim 1$ $M_\odot$, nonpulsating giants in RS Oph and T CrB.

Our spectra of RS Oph show the presence of the Li I line, and the radial velocities of this line fit very well to the M-giant radial velocity curve (see right panel Fig. 7). The identification of the weak and narrow absorption line at 6706–6708 Å with Li I λ6708 is unambiguous since no other neutral element following the giant motion has a strong transition at that wavelength. In addition, the presence of this line is clearly seen in the higher resolution Feros spectra. The feature was observed in all our spectra, except in April 2006 where all the absorption lines were overwhelmed by very strong blue continuum from the nova outburst.

This result indicates that, regardless of the mechanism involved to generate lithium, it should operate within the cool giant atmosphere. The observed Li would be the initial Li (which is observed in non convective stars) if some process operating in such binary systems as RS Oph and T CrB, e.g. delayed onset of convection or a lack of differential rotation due to tidal locking, can inhibit lithium depletion (Shabhaz et al. 1999).

Wallerstein et al. (2008) offered another possibility for the presence of Li. They suggested that it is freshly created in the interior and convected to the surface. They also noted that some G and K-type giants have very high atmospheric Li abundances. In the case of these Li-rich giants, Charbonnel & Balachandran (2000) identified two distinct episodes of Li production occuring
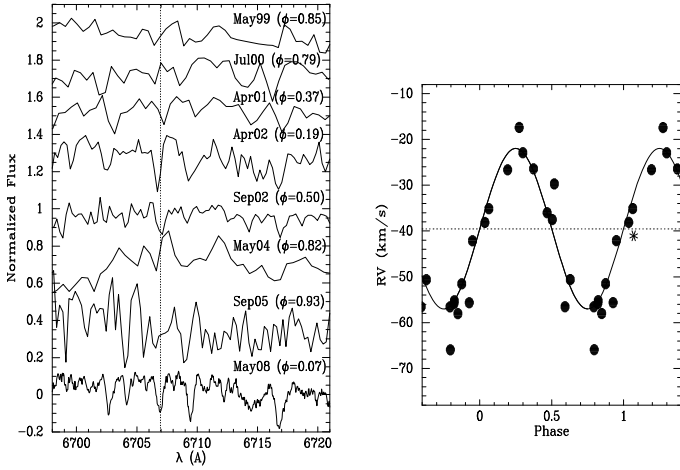
Fig. 7. (*Left*) Presence of the Li ɪ $\lambda6707$ absorption line in RS Oph during quiescence. The dotted line indicates the position of the line corrected by the baricentric velocity of the binary. (*Right*) The radial velocities of Li ɪ following the M-giant motion. Filled circles, Casleo data and asterisk, Feros data. The solid line gives the circular solution for the M-giant, as in Fig. 1.

in advanced evolutionary phases depending upon the mass of the star. Low-mass RGB stars which later undergo a helium flash produce Li at the start of the red giant luminosity bump phase whereas in intermediate-mass stars the Li-rich phase occurs when the convective envelope deepens at the base of the AGB. The position of the cool giant of T CrB in the HR diagram is consistent with a low-mass, $\sim 1\ M_\odot$, star at the top of the RGB whereas the location of RS Oph is consistent with such a giant only if its metallicity is significantly subsolar (Mikołajewska 2008), and in both cases the stars are located far from the RGB bump. On the other hand, Wallerstein et al. (2008) found a normal, nearly solar, ratio of metals to hydrogen in both RS Oph and T CrB, and they concluded that the giant component has not yet lost sufficient mass to make its atmosphere deficient in hydrogen. It seems therefore unlikely that the initial mass of the M giant was significantly greater than its current estimate of $0.68-0.8\ M_\odot$.

An alternative explanation is the pollution of the giant by the nova ejecta. This explanation has, however, some weak points. In particular, the red giant should very efficiently accrete the Li-rich material ejected at very high velocity (a few $1000\ \mathrm{km\,s^{-1}}$!) to be significantly polluted. Moreover there is also serious controversy about the production of Li during such an explosion.

5. RS Oph in 2006

High-dispersion spectra of RS Oph were taken at CASLEO with the same instrumental configuration on 2006 April 7–8 and October 12, that is, 54–55 and 240 days following the explosion. The spectra of April show broad emission lines of hydrogen recombination lines, together with He ɪ, He ɪɪ, Fe ɪɪ, N ɪɪɪ, [O ɪ] $\lambda6300$, [O ɪɪɪ] $\lambda5007$, [N ɪɪ] $\lambda5754$ and the Raman band at $\lambda6825$ Å. The cF absorption system is not observed in April 2006. Very narrow emission components are seen on top of the broad emission components.

Strong coronal emission lines such as [Fe xɪv] $\lambda5305$, [A x] $\lambda5535$ and [Fe x] $\lambda6375$ (Fig. 8) are also present, showing the same structure in the profiles. Our measures of the integrated fluxes, the radial velocity of the emission line components and
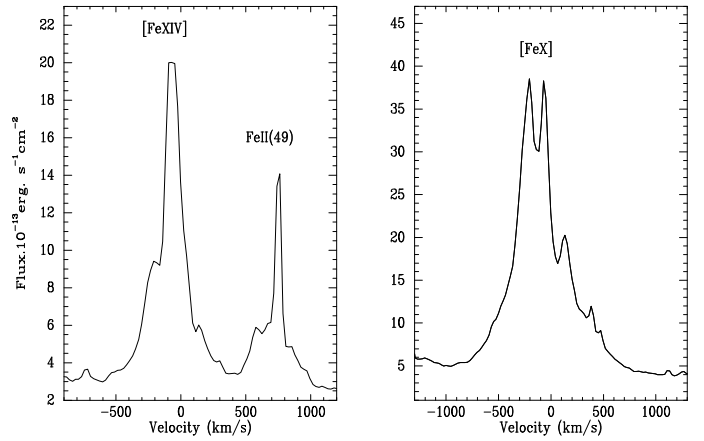

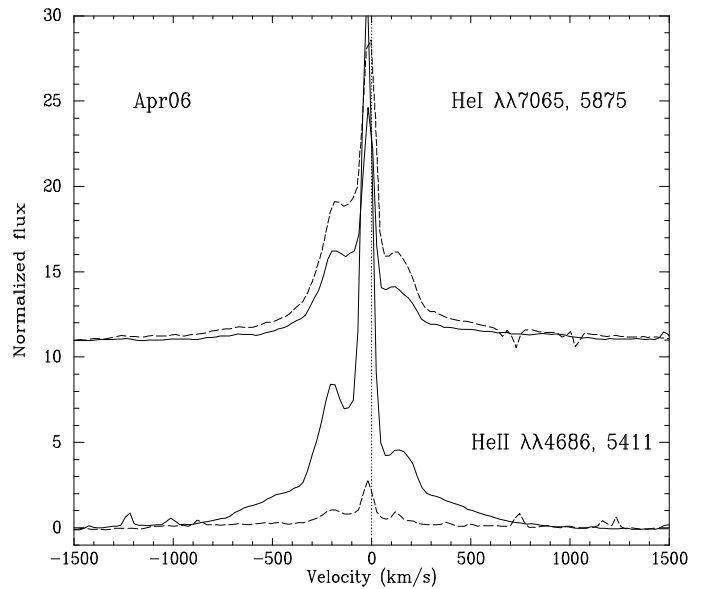**Fig. 8.** Observed coronal lines in RS Oph on April 2006.

Fig. 9. The He ɪ and He ɪɪ profiles showing a broad pedestal with the strong narrow component at -15 and $-23\ \mathrm{km\,s^{-1}}$ respectively. Two separate emission components of higher radial velocity at -200 and $+150\ \mathrm{km\,s^{-1}}$ are observed, the blue component being stronger than the red one.

the full width at zero intensity (FWZI) of several stronger lines are shown in Table 4.

Most of the emission lines present a strong and narrow component with a radial velocity between -14 and $-25\ \mathrm{km\,s^{-1}}$ and two other components extended to the blue and the red side. In the cases of the [N ɪɪ] and [O ɪɪɪ] emission lines and the coronal lines, the radial velocity of the narrow component is more negative (-40 and $-50\ \mathrm{km\,s^{-1}}$).

We can see in Fig. 9 the He ɪ $\lambda\lambda5875, 7065$ and He ɪɪ $\lambda4686$, 5411 profiles showing a broad pedestal with the strong narrow component at -15 and $-23\ \mathrm{km\,s^{-1}}$ respectively. Two separate emission components of higher radial velocity are observed at ~ -200 and $+150\ \mathrm{km\,s^{-1}}$ with the blue component stronger than the red one. An explanation based on a bipolar gas outflow may be applicable to the presence of these components with expanding and receding radial velocities.

On October 2006, the RS Oph spectrum is slowly restoring its quiescent characteristics. The cF-absorption system, absent in April 2006, has reappeared. The intensity of the emission lines decreases, the coronal lines are not observed and the blue and

Table 4. Emission lines of RS Oph on April 2006.

Species	λ [Å]	Flux (10^{-12}) (erg s^{-1} cm^{-2})	RV (km s^{-1}) narrow	RV (km s^{-1}) blue	RV (km s^{-1}) red	FWZI (km s^{-1})
H I						
Hβ	4861	59.1	−21	−38		2500
Hα	6562	460	−47			3840
P23	8345	0.6	−19			
P22	8359	1.0	−20			
P21	8374	1.0	−23			
P20	8392	1.3	−20			
P19	8413	2.2	−16			
He I						
	4471	2.6	−19	−205	81	1100
	5875	25.4	−14	−194	155	1950
	6678	9.4	−15	−208		740
	7065	28.1	−17	−196	156	1400
He II						
	4686	26.7	−25	−209	164	1680
	5411	3.4	−21	−208	122	1050
Fe II						
M27	4233	1.9	−20	−186		800
M38	4583	1.7	−20	−272:	77w	650
M42	5169	2.3	−20	−121	123w	580
M49	5234	1.4	−22	−124	134	720
M49	5316	2.4	−18	−195	88w	580
M74	6247	0.8	−22	−141	47	514
M73	7711	1.7	−24	−122	181	717
Raman band	6825	5.1				1470
Forbidden lines						
[O I]	6300	0.6	−15	−94	90	350
[N II]	5754	4.6	−42		81	925
[O III]	5007	1.7	−40	−104		320
Coronal lines						
[Fe XIV]	5303	7.0	−52	−220	163w	900
[A X]	5535($\star$)	7.5	−13	−282	100w	1930
[Fe X]	6375	35.1	−40	−188	166	1500

w: very weak line.
($\star$): blend with Fe IIλ5534.9.

red components of the He I lines have disappeared. Hα has recovered its pre-outburst profile, in particular the emission wings are narrower than in April 2006 and the emission is cut by an incipient central absorption (see Fig. 4). A very weak He II λ4686 line is still observed, although its flux has decreased by a factor of ~90 with respect to that of April 2006. This profile preserves the strong emission component at −46 km s^{-1} and two expanding components at −214 and +192 km s^{-1}, with the red component being stronger than the blue one, that is, in the opposite sense of that of April (Fig. 10, left panel).

6. Conclusions

1. We have re-determined the spectroscopic orbits of RS Oph based on the radial velocity curve of the M-type absorption lines at wavelengths longer than 6000 Å. As the H I broad emission wings seem to follow the hot component motion, combined orbital solutions for both components were also determined with a period of 453.6 days, very similar to those given by FJHS00. We conclude, as DK94 do, that the cF-type absorption lines are not associated with either binary component, and are most likely formed in the material streaming towards the hot component.
   Assuming a massive white dwarf as the hot component of the system ($M_\mathrm{h} = 1.2-1.4\,M_\odot$) the red giant mass results in $M_\mathrm{g} = 0.68-0.80\,M_\odot$ and the orbit inclination, $i = 49°-52°$.

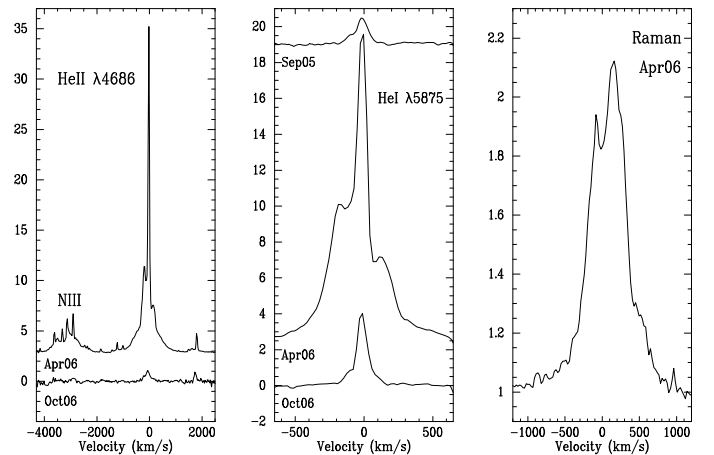**Fig. 10.** *Left panel*: N III emission lines observed in April 2006. The He IIλ4686 is still detected on 2006 October 12. *Middle panel*: intensity and profile variations of He Iλ5875 before and after explosion. *Right panel*: the scattering Raman band at 6825 A, which does not appear at all during the quiescent phase, is present as a strong emission profile in April 2006. This feature is not observed in October 2006.

2. During the quiescent period of our observations the spectra of RS Oph show variability in the fluxes of the emission lines and in the continuum. A correlation of the H I and He I

emission line fluxes with the monochromatic magnitudes at 4800 Å was obtained, indicating that the hot component activity is responsible for those flux variations.

3. Our spectra of RS Oph reveal the presence of the Li I 6708 line, and the radial velocities of this line fit the M-giant radial velocity curve very well. This result indicates that, whatever the mechanism involved to generate lithium would be, it should operate within the cool giant atmosphere. An alternative explanation is the pollution of the giant by the nova ejecta but the red giant in this case should very efficiently accrete the Li-rich material ejected at very high velocity to be significantly polluted.

4. We present the characteristics of the spectra around 54–55 and 240 days after the outburst of February 2006. On April 2006 most of the emission lines present a broad pedestal with a strong and narrow component at about -20 km s^{-1} and two other extended emission components at -200 and $+150$ km s^{-1}. These components could originate in a bipolar gas outflow supporting the model of a bipolar shock-heated shell expanding through the cool component wind and perpendicular to the orbital plane of the binary.

5. Our observations indicate that the cF system was disrupted during the outburst. The cF absorption lines were not observed in our spectra in April 2006 and Zamanov et al. (2006) reported the absence of flickering in June 2006, then the accretion was not yet resumed immediately after the outburst. Both the cF system and the flickering (Worters et al. 2007) were observed again about 240 days after the outburst, which is consistent with the resumption of accretion in RS Oph.

References

Anupama, G. C., & Mikołajewska, J. 1999, A&A ,344, 177
Barry, R. K., Mukai, K., Sokoloski, J., et al. 2008, in the Proceedings of the Meeting, RS Ophiuchi (2006), ed. N. Evans, M. Bode, & Tim O'Brien, ASP Conf. Ser., 401
Brandi, E., Mikołajewska, J., Quiroga, C., et al. 2005, A&A, 440, 239
Charbonnel, C., & Balachandran, S. C. 2000, A&A, 359, 563
Dobrzycka, D., & Kenyon, S. 1994, AJ, 108, 2259
Fekel, F. C., Joyce, R. R., Hinkle, K., & Skrutskie, M. F. 2000, AJ, 119, 1375
Garcia, M. 1986, AJ, 91, 1400
Hamuy, M., Walker, A. R., Suntzeff, N. B., et al. 1992, PASP, 104, 533
Hamuy, M., Suntzeff, N. B., Heathcote, S. R., et al. 1994, PASP, 106, 566
Jordi, J. 2005, NuPhA, Nucl. Phys. A, 758, 713
Lucy, L. B., & Sweeney, M. A. 1971, AJ, 76, 544
Martin, E. L., Rebolo, R., Casares, J., & Charles, P. A. 1994, ApJ, 435, 791
Mikołajewska, J. 2008, in the Proceedings of the Meeting: RS Ophiuchi (2006), ed. N. Evans, M. Bode, & Tim O'Brien, ASP Conf. Ser., 401
Mikołajewska, J., & Kenyon, S. J. 1992, AJ, 103, 579
Mikołajewska, J., & Kenyon, S. J. 1996, AJ, 112, 1659
Mikołajewska, J., & Mikołajewski, M. 1988, in The Symbiotic Phenomenon, ed. J. Mikołajewska, M. Friedjung, S. J. Kenyon, & R. Viotti (Dordrecht: Kluwer), 187
Oppenheimer, B., & Mattei, J. A. 1993, BAAS, 25, 1378
Quiroga, C., Mikołajewska, J., Brandi, E., et al. 2002, A&A, 387, 139
Schneider, D. P., & Young, P. 1980, ApJ, 238, 946
Shabhaz, T., Hauschildt, P., Naylor, T., & Ringwald, F. 1999, MNRAS, 306, 675
Tatarnikova, A. A., Marese, P. M., Munari, U., et al. 2003, MNRAS 344, 1233
Wallerstein, G., Harrison, T., & Munari, U. 2006, BAAS, 38, 1160
Wallerstein, G., Harrison, T., Munari, U., & Vanture, A. 2008, PASP, 120, 492
Worters, H. L., Eyres, S. P. S., Bromage, G. E., & Osborne, J. P. 2007, MNRAS, 379, 1557
Zahn, J.-P. 1977, A&A, 57, 383
Zamanov, R., Panov, K., Boer, M., & Coroller, H., Le 2006, The Astronomer's Telegram, 832
Zamanov, R. K., Bode, M. F., Melo, C. H. F., et al. 2007, MNRAS, 380, 1053